Modeling the Motion of Microrobots on Surfaces Using Nonsmooth Multibody Dynamics

Zoltán Nagy, Remco I. Leine, Dominic R. Frutiger, *Member, IEEE*, Christoph Glocker,
and Bradley J. Nelson, *Fellow, IEEE*

***Abstract*—We apply nonsmooth multibody dynamics to describe the motion of a microrobot which is driven by the wireless resonant magnetic microactuator. We first analyze the robot using a simplified analytical model, which allows us to derive characteristic and nondimensional parameters that describe its dynamics. We then perform a numerical study to analyze the nonlinearities. We predict several nonintuitive phenomena, such as switching of the direction of the velocity with changing excitation frequency, and show that both erratic and controlled motions occur under specific conditions. Our numerical results are qualitatively consistent with experimental observations and indicate that previous speculations on the motion mechanism were incorrect. The modeling method is general and readily applies to other microrobots as well.**

***Index Terms*—Animation and simulation, contact modeling, dynamics, micro/nano-robots, smart actuators.**

I. Introduction

Many technologies must be developed and synergistically integrated in order to realize microrobots for the real world [1]. Aspects that must first be addressed for wireless mobile microrobotic platforms are power supply and propulsion. These aspects are challenging since both onboard batteries and classical wireless power transmission using, e.g., electromagnetic coupling between coils are inefficient for microdevices due to scaling effects [2]. As a result, microrobotic systems that feature wirelessly controlled agents with principle dimensions in the submillimeter range have only emerged in recent years [3]–[10]. Some of these developments follow a bioinspired approach, trying to mimic the rotational motion of bacterial flagella which in turn drives the robot forward inside a liquid [9], [10].

Other approaches, especially to move on substrates, use increasingly complex mechanical structures and motion mechanisms for propulsion. The electrostatic microrobot that is proposed in [3] is an untethered version of the scratch drive actuator introduced in [11]. The system uses a substrate with individually addressable electrodes to capacitively couple the polysilicon microrobot to it and thereby induce linear sliding motion. Then, by adding a cantilevered steering arm that can be fixed selectively to the substrate, the same group demonstrated arbitrarily steerable electrostatic microrobots on a planar surface [12] and multiple individually controllable planar microrobots in [13].

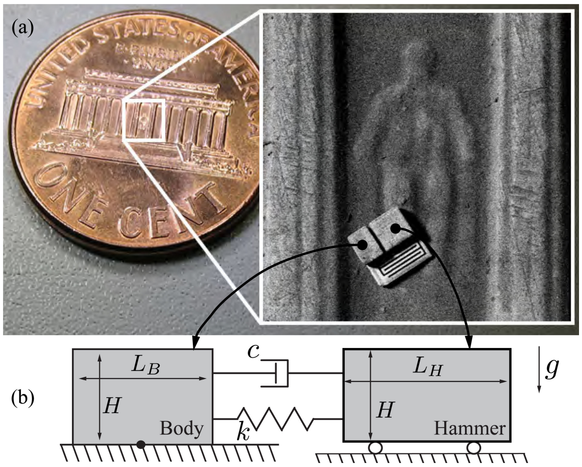

Fig. 1. (a) WRMMA in size comparison with a U.S. penny. (b) 1-D mechanical model of the WRMMA (see Section II-A).

The stick/slip microrobot Mag-μBot that is presented in [8] is a small NdFeB magnet $250 \times 130 \times 100\,\mu\text{m}^3$ and is actuated on a substrate surrounded by three orthogonal pairs of electromagnets. Actuation is achieved by imposing a time-varying magnetic torque on the microrobot which then pivots over the substrate in a stick/slip manner. Global positioning of several of these microrobots has also been recently demonstrated [14].

The wireless resonant magnetic microactuator (WRMMA) introduced in [7] and [15] is shown in Fig. 1(a). The WRMMA consists of two nickel masses that are connected through a gold spring and has overall dimensions of roughly $300 \times 300 \times 50\,\mu\text{m}^3$. As shown in Fig. 1(b), one mass, i.e., the body, rests on a gold frame support structure, i.e., on the substrate, whereas the other mass, i.e., the hammer, is located above the substrate and can move freely without friction. An oscillating magnetic field induces a time-varying attractive magnetic force between the hammer and the body. This leads to their oscillatory motion resulting in observable propulsion of the WRMMA. Because of the low masses, the actual motion mechanism is not clear as the oscillations are in the kilohertz range and, thus,

Manuscript received June 30, 2011; revised January 19, 2012; accepted May 6, 2012. Date of publication June 1, 2012; date of current version September 28, 2012. This paper was recommended for publication by Associate Editor M. Sitti and Editor G. Oriolo upon evaluation of the reviewers' comments.

Z. Nagy was with the Institute of Robotics and Intelligent Systems, Department of Mechanical and Process Engineering, ETH Zurich, 8092 Zurich, Switzerland. He is now with the Institute of Technology in Architecture, Department of Architecture, ETH Zurich, 8092 Zurich, Switzerland (e-mail: nagyz@ethz.ch).

D. R. Frutiger and B. J. Nelson are with the Institute of Robotics and Intelligent Systems, Department of Mechanical and Process Engineering, ETH Zurich, 8092 Zurich, Switzerland (e-mail: nagyz@ethz.ch; dfrutiger@ethz.ch; bnelson@ethz.ch).

R. I. Leine and C. Glocker are with the Institut für Mechanische Systeme, Department of Mechanical and Process Engineering, ETH Zurich, 8092 Zurich, Switzerland (e-mail: remco.leine@imes.mavt.ethz.ch; christoph.glocker@imes.mavt.ethz.ch).

Color versions of one or more of the figures in this paper are available online at http://ieeexplore.ieee.org.

Digital Object Identifier 10.1109/TRO.2012.2199010

cannot be observed experimentally. It was speculated that the impact between the body and the hammer causes the motion [7], [15]. See [16] for a recent demonstration of the capabilities of the WRMMA.

These microrobot examples rely on complex mechanical phenomena such as sliding, stiction, and impact. These interactions are complex to model due to their nonsmooth nature. Three main approaches exist to analyze such systems. First, regularizing the friction force by an $\arctan$ function transforms its nonsmooth nature into an analytical function that can be used in the equations of motion. The drawback is that the physics are modeled inaccurately as stiction, and thus, stick↔slip transitions cannot be captured. This approach is often employed in animations and computer games where physical accuracy is not important. Second, if nonsmoothness is preserved, event-driven algorithms can be employed, as shown in [8], to model pivoting stick/slip motion. This procedure yields the correct results and is practical for a single contact point. However, at each time step a logic decision tree must be created in order to identify the stiction/sliding state of the system. Consequently, the method becomes complex and error prone for problems with multiple contact points as is the case for the scratch drive actuator or the WRMMA.

To overcome these limitations, significant advances have been made over the past two decades, and it has become possible to formulate the contact problem and the nonsmooth phenomena in a physically consistent, mathematically sound, and numerically stable way [17]. In particular, Moreau's time-stepping algorithm has been employed with great success [18]–[22], and nonsmooth multibody methods with set-values force laws have recently been applied to various engineering problems in robotics [23], haptics [24], and electronics [25].

This paper introduces the nonsmooth multibody dynamics method with set-valued force laws to model the motion of microrobots on surfaces. As detailed previously, direct observation of the nonsmooth phenomena at the microscale is impossible, and thus, an accurate physical model is indispensable to analyze the dynamics. In addition, a numerical model permits exploration of the parameter space and predicts nonintuitive, interesting phenomena. Using the WRMMA, we show how our approach seamlessly models multiple contact points and predicts and explains nonintuitive yet experimentally observed phenomena.

Previous work on the WRMMA presented experimental results, yet did not attempt to model the motion mechanism [7], [15]. Preliminary numerical results on the motion of the WRMMA were given in [26]. The contributions of this paper are the derivation and analysis of the analytical model of the WRMMA in Section II, the formulation of its nonsmooth dynamics model and an extensive numerical study in Section III, and the analysis of the results in Section IV. We conclude this paper in Section V.

II. WIRELESS RESONANT MAGNETIC MICROACTUATOR

A. System Overview

The magnetic torque on the WRMMA acts such that the easy axis of the device, typically the long axis (but it could be a diagonal), aligns with the applied field. Since rotational inertia scales down faster with size compared to mass, we assume that the linear motion begins after the WRMMA is aligned with the field. Thus, a 1-D model is employed to describe its motion.

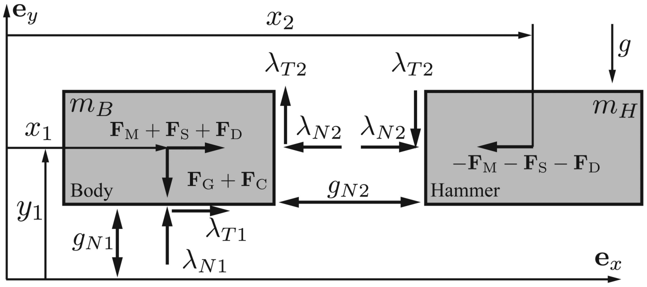

Fig. 2. Free-body diagram of the WRMMA.

Fig. 2 shows the free-body diagram of the WRMMA. The position of the body is described with coordinates (x_1, y_1), and the hammer is described with coordinate x_2. Note that y_1 is only necessary for consistency in the numerical integration procedure. The terms λ_{Ni} and λ_{Ti} in Fig. 2 designate normal and tangential nonimpulsive contact forces, respectively (see Section III).

1) Mass, Spring, and Damper: The size of the device is roughly $300 \times 300 \times 50\,\mu\mathrm{m}^3$. In the first prototypes, the body and the hammer each had a length of about $150\,\mu$m, a width of $130\,\mu$m, and a height of $50\,\mu$m [7]. The density of nickel is $\rho_\mathrm{Ni} = 8900\,\mathrm{kg/m}^3$, which results in a mass on the order of 10×10^{-9} kg for each part. Experimental characterization and the determination of the parameter values that are used in the following have been carried out in [15] and [27].

As for modeling the geometry, we consider devices with asymmetrical mass distribution. We denote by m_B the mass of the body and by $m_H = \alpha\, m_B$ the mass of the hammer, where $\alpha = m_H/m_B$ is the mass ratio. We assume the same width and height for the body and the hammer, only the lengths differing. We consider a total device length of $L_\mathrm{device} = L_H + L_B + g_0 = 300\,\mu$m, where L_H and L_B are the lengths of the hammer and the body, respectively, and g_0 is the equilibrium gap [see (2)]. Because of equal height and width, we have $L_H = \alpha L_B = \alpha(L_\mathrm{device} - g_0)/(1+\alpha)$.

Neglecting the mass of the spring and the frame, the total mass m_T of the device is $m_T = m_B + m_H = (1+\alpha)m_B$, and the gravitational force $\mathbf{F_G}$ that acts on the WRMMA is given by

$$\mathbf{F}_G = -F_G\,\mathbf{e}_y = -\beta(1+\alpha)m_B\,g\,\mathbf{e}_y \tag{1}$$

where $g = 9.81\,\mathrm{kg/m}^2$, and $\beta > 0$ is a nondimensional parameter to study the effect of unknown vertical forces, such as additional mass due to the gold frame and spring or parasitic electrostatic forces, leading to changing frictional behavior.

The spring stiffness k is linear; thus, the spring force that acts on the body is given by

$$\mathbf{F}_S = F_S\,\mathbf{e}_x = k\,g_{N2}\,\mathbf{e}_x \tag{2}$$

where $g_{N2} := x_2 - x_1 - g_0$ is the gap between the body and the hammer, g_0 is the gap at rest, and $k = 10.6\,\mathrm{N/m}$ represents a typical stiffness value [27].

For the damping force $\mathbf{F}_D$, we assume linear drag behavior

$$\mathbf{F}_D = F_D\,\mathbf{e}_x = c\,\dot{g}_{N2}\,\mathbf{e}_x \tag{3}$$

with $\dot{g}_{N2} = (\dot{x}_2 - \dot{x}_1)$ being the relative velocity of the body and the hammer, and $c \approx 1 \times 10^{-6}$ Ns/m is a typical drag coefficient in air [27].

2) Magnetic Force: In a homogeneous magnetic field, no net force is exerted on a single, ideally soft, magnetic body because of the lack of magnetic field gradients. Thus, the force between the parts of the WRMMA arises solely due to the interaction of both magnetizations. Standard results are only available for the expression of the force between two hard magnetic bodies as their magnetizations are independent and superpositions holds [28]. There is no prior work on calculating the magnetic force between two nearby soft-magnetic bodies when placed in an external magnetic field. Here, we derive an expression which is based on finite element (FE) results.

The two nickel parts act as a magnetic flux concentrator, amplifying the applied magnetic flux $\mathbf{B}$ in the air gap between them, i.e., $B_{\text{gap}} = A_m(g_{N2})\mathbf{B}$ with $A_m(g_{N2})$ being the amplification factor. The magnetic energy in a sufficiently small air gap with volume $V = A \cdot g_{N2}$, where A is the facing pole area, is given by

$$E_{\text{gap}} = \frac{1}{2}\int_V B_{\text{gap}} H_{\text{gap}}\,\mathrm{d}V = \frac{A\|\mathbf{B}\|^2}{2\mu_0} g_{N2} A_m^2(g_{N2}) \tag{4}$$

with $H_{\text{gap}} = B_{\text{gap}}/\mu_0$. From the energy, the force on the body (and on the hammer) is determined as

$$\mathbf{F}_M = -\frac{\mathrm{d}E_{\text{gap}}}{\mathrm{d}g_{N2}}\,\mathbf{e}_x \tag{5}$$

$$= -\frac{A\|\mathbf{B}\|^2}{2\mu_0} A_m^2(g_{N2}) \left(1 + \frac{2g_{N2}}{A_m(g_{N2})}\frac{\mathrm{d}A_m(g_{N2})}{\mathrm{d}g_{N2}}\right)\mathbf{e}_x. \tag{6}$$

The amplification factor $A_m(g_{N2})$ is approximated as [29]

$$A_m(g_{N2}) = \frac{c_g \mu_{\text{eff}} + \tilde{g}_{N2}}{c_g + \tilde{g}_{N2}} \tag{7}$$

where $\tilde{g}_{N2}$ is the gap normalized with the total magnetic length of the device, i.e., $\tilde{g}_{N2} = g_{N2}/(L_H + L_B)$, c_g is a geometry-dependent fit factor, and μ_{eff} is the effective permeability. Because of the small scale, μ_{eff} is shape dominated, and we have $\mu_{\text{eff}} \approx 1/n_x$ [30]. The demagnetizing factor n_x has to be calculated for the device with magnetic length $L_H + L_B$. Using the procedures from [31], we find $n_x = 0.1161$.

For the fit factor c_g, since a numerical, i.e., FE, fit has to be used to determine its value, we simplify the force expression by replacing the expression in the brackets in (6) by a fit factor κ^2 and modify the amplification factor as

$$A_\kappa^2(g_{N2}) := \frac{c_g \mu_{\text{eff}} + \tilde{g}_{N2}}{(c_g + \tilde{g}_{N2})^2} = \frac{A_m^2(g_{N2})}{c_g \mu_{\text{eff}} + \tilde{g}_{N2}}. \tag{8}$$

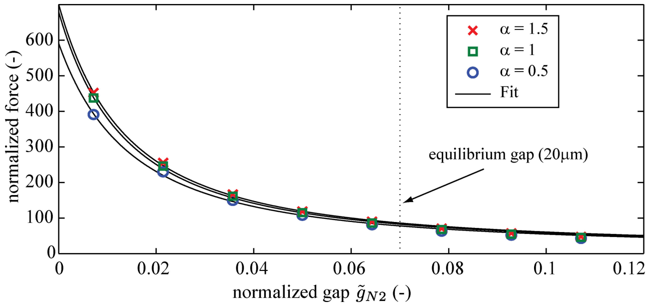

Fig. 3. FE results and fit of the normalized magnetic force for different mass ratios α.

This form has been found through observing the numerical fit with respect to the FE results, and thus, (6) takes the more compact form

$$\mathbf{F}_M = -\frac{A\|\mathbf{B}\|^2}{2\mu_0}\kappa^2 A_\kappa^2(g_{N2})\mathbf{e}_x. \tag{9}$$

The applied magnetic field $\mathbf{B}$ is modeled as a square signal with frequency f_a, amplitude B, and offset $\mathcal{B}$, i.e.,

$$\mathbf{B}(t) = \frac{1}{2}B(\operatorname{sgn}(\sin(2\pi f_a t)) + \mathcal{B}) \tag{10}$$

where $\operatorname{sgn}(\cdot)$ is the signum function. It is difficult to experimentally achieve a square magnetic field signal due to the low-pass characteristic of the electromagnetic coils used to generate it, and the actual signal has a rather trapezoidal form [27]. The investigation of the influence of the signal form is beyond the scope of this study. We opt to study the idealized on/off square wave ($\mathcal{B} = 1$), as this is the desired signal and the theoretical limit for the actuation of the WRMMA.

Finally, by inserting (10) into (9), we obtain the time-varying magnetic force between the body and the hammer as

$$\mathbf{F}_M(g_{N2}, t) = \frac{A\|\mathbf{B}(t)\|^2}{2\mu_0}\kappa^2 A_\kappa^2(g_{N2})\,\mathbf{e}_x \tag{11}$$

$$= \underbrace{\frac{AB^2}{8\mu_0}\kappa^2 A_\kappa^2(g_{N2})}_{:=F_M(g_{N2})}(\operatorname{sgn}(\sin(2\pi f_a t)) + \mathcal{B})^2\,\mathbf{e}_x \tag{12}$$

and the influence of the shape on the magnitude of the force can be analyzed with $\mathcal{B} = 1$ and $t = 0$ by normalizing as

$$\frac{8\mu_0\|\mathbf{F}_M\|}{AB^2} = \kappa^2 A_\kappa^2(g_{N2}). \tag{13}$$

To determine the fit parameters c_g and κ, we perform an FE analysis (Ansoft Maxwell 3Dv13) with $\mu_r = 600$ as the permeability value for bulk nickel, which is sufficiently high to neglect the influence of the material, and the mass ratios $\alpha = \{0.5, 1, 1.5\}$. The FE results and the excellent fit are shown in Fig. 3. The fit parameters are constant over varying α and summarized in Table I.

We observe in Fig. 3 that the curves differ only slightly for different mass ratios. This is important for experimental design, as it shows that as long as the magnetic volume is the same, the magnetic force between the body and the hammer remains similar. This means that fabrication imperfections, resulting in

TABLE I
FIT PARAMETERS AND GOODNESS OF FIT VALUES FOR THE NORMALIZED MAGNETIC FORCE SHOWN IN FIG. 3

α	c_g	κ	RMSE	R^2
0.5	0.027	2.823	7.032	0.997
1	0.025	3.074	6.768	0.998
1.5	0.025	3.028	6.740	0.998

slightly different magnetic volume, will still yield the same force between the body and the hammer, and thus, effects that result from a different force can be excluded. Since the mass influences the resonant frequency of the device, this result shows that it is possible to change the resonant behavior of the device while keeping the same interaction force.

3) Electrostatic Clamping Force: Below the substrate with thickness d_S on which the microrobot is moving is a set of electrodes that can be set to a specific electrostatic potential $V_C(t)$. This results in charge separation in the gold frame of the robot, and, consequently, in an electrostatic clamping force $\mathbf{F}_C$ that acts vertically on the body [27]

$$\mathbf{F}_C = -F_C(t)\,\mathbf{e}_y = -\epsilon\frac{A_S V_C^2(t)}{2d_S^2}\,\mathbf{e}_y \tag{14}$$

where A_S is the area of the WRMMA facing the substrate, and ϵ is the dielectric constant of the substrate. The potential $V_C(t)$ is an on/off signal which is shifted by a phase $\varphi \in [-\pi/2, \pi/2]$ with respect to the magnetic signal [see (10)], i.e.,

$$V_C(t) = \frac{1}{2}V_{C0}(\operatorname{sgn}(\sin(2\pi f_a t + \varphi)) + 1) \tag{15}$$

which leads to the clamping force magnitude

$$F_C(t) = F_{C0}(\operatorname{sgn}(\sin(2\pi f_a t + \varphi)) + 1)^2 \tag{16}$$

with $F_{C0} = (1/8)\epsilon A_S V_{C0}\, d_S^{-2}$. The precise value of F_{C0} is not important. For the simulations, it is chosen sufficiently high ($F_{C0} = 1\,\mathrm{N}$) such that the body sticks to the substrate.

B. Linear Model for the Dynamics

For a first insight into the motion principle of the WRMMA, we analyze its equations of motion analytically. Then, we give the solution for stiction, as well as the conditions for stick↔slip transitions, and analyze the sliding motion briefly.

1) Assumptions: To simplify the expressions, we neglect damping, and assume that the magnitude of the magnetic force is constant and independent of the gap size. We do not consider clamping, focusing instead on the natural motion principle. A sinusoidal magnetic field is assumed using the first term of the Fourier expansion of the square wave:

$$\operatorname{sgn}(\sin(2\pi f_a t)) = \frac{4}{\pi}\sum_{k=1}^{\infty}\frac{\sin((2k-1)2\pi f_a t)}{2k-1} \tag{17}$$

$$= \frac{4}{\pi}\left(\sin(2\pi f_a t) + \frac{1}{3}\sin(6\pi f_a t) + \cdots\right) \tag{18}$$

and the resulting force $\mathbf{F}_M(t) = F_M(t)\mathbf{e}_x$ is

$$F_M(t) = \underbrace{\frac{AB^2}{8\mu_0}\kappa^2 A_\kappa^2(g_0)}_{:=F_0}\underbrace{\left(\frac{4}{\pi}\sin(2\pi f_a t) + \mathcal{B}\right)^2}_{:=f(t)}. \tag{19}$$

2) Equations of Motion: When both the body and the hammer are moving, the system is described by the following system of two coupled second-order differential equations:

$$\begin{cases} m_B\ddot{x}_1(t) = F_S + F_M(t) + F_T(\dot{x}_1(t)) \\ m_H\ddot{x}_2(t) = -F_S - F_M(t) \end{cases} \tag{20}$$

where the friction force F_T is set-valued and described by an inclusion

$$F_T(\dot{x}_1) \in -\mu F_G \operatorname{sgn}(\dot{x}_1) \tag{21}$$

or, equivalently

$$F_T(\dot{x}_1) = \begin{cases} -\mu F_G, & \dot{x}_1 > 0 \\ [-1, 1]\mu F_G & \dot{x}_1 = 0 \\ \mu F_G, & \dot{x}_1 < 0 \end{cases} \tag{22}$$

assuming for simplicity that the friction coefficient μ is the same for static and kinetic friction.

The advantage of the set-valued force law is now apparent. If the sgn function is regularized, or smoothened, by some arctan function to obtain an equation rather than an inclusion, the slope around $\dot{x}_1 = 0$ will be very steep causing numerically stiff equations. In addition, and worse, the body can never stick, and hence, the physics are not correctly modeled. In contrast, a set-valued friction law (22) allows one to clearly define the motion states and the transition conditions as

$$\dot{x}_1 = 0\,(\text{stiction}) \Rightarrow \begin{cases} \text{body sticks as long as } |F_T| < \mu F_G \\ \text{body sticks until } |F_T| = \mu F_G \\ (\text{stick} \rightarrow \text{slip transition}) \end{cases} \tag{23}$$

$$\dot{x}_1 \neq 0\,(\text{sliding}) \Rightarrow \begin{cases} \text{body slides as long as } \dot{x}_1 \neq 0 \\ \text{body slides until } \dot{x}_1 = 0 \\ (\text{slip} \rightarrow \text{ stick transition}) \\ \qquad\qquad\quad \textbf{or} \\ \text{body keeps sliding: } \dot{x}_1 \neq 0 \\ (\text{forward} \leftrightarrow \text{ backward slip transition}). \end{cases} \tag{24}$$

To derive the characteristic parameters of the system, we nondimensionalize the equations of motion as follows. We define

$$s(t) := x_1(t) + x_2(t), \text{and } d(t) := x_2(t) - x_1(t) - g_0 \tag{25}$$

and introduce the nondimensional parameters σ, δ, τ, and η, and the characteristic parameters s_c, d_c, and t_c as

$$t = t_c\tau, \quad s(t) = s_c\sigma(\tau), \quad d(t) = d_c\delta(\tau), \quad \eta = \frac{d_c}{s_c} \tag{26}$$

and

$$\frac{1}{t_c} = \sqrt{\frac{k}{m_H}} = \omega_1 = 2\pi f_1, \quad d_c = \frac{F_0}{k}, \quad \eta = \frac{F_0}{\mu F_G} \tag{27}$$

where ω_1 and f_1 are the natural frequency of the hammer-spring oscillator (keeping the body fixed or tethered) in radians per second and Hertz, respectively. The characteristic displacement d_c represents the change of the gap given the magnetic force and the spring since $F_0 = kd_c$. Finally, η is a nondimensional parameter that represents the ratio of the maximum magnetic force to the maximum friction force and is a key parameter for the design and actuation of the WRMMA. With the definitions for the forces of the previous section and noting that $F_M(t) = F_0 f(t)$ [see (19)], the nondimensional inclusion version of the system (20) is derived as

$$\begin{cases}\ddot{\sigma}(\tau) - (\alpha-1)\eta\delta(\tau) \in (\alpha-1)\eta f(\tau) - \alpha\gamma(\tau)\\ \ddot{\delta}(\tau) + (\alpha+1)\delta(\tau) \in -(\alpha+1)f(\tau) + \frac{\alpha}{\eta}\gamma(\tau)\end{cases} \tag{28}$$

with $\gamma(\tau) := \operatorname{sgn}(\dot{\sigma}(\tau) - \eta\dot{\delta}(\tau)) \in [-1, 1]$. For the remainder of this paper, the dot represents differentiation with respect to the nondimensional time τ.

As long as the nondimensional parameters remain constant, the effects of individual parameters on the overall performance of the system, e.g., the velocity of the robot, may compensate each other. Thus, care must be taken during the experimental investigation to isolate individual effects. We now investigate the special cases of stiction, i.e., stick→slip transitions and sliding.

3) Solution for Stiction (Tethered case: $\dot{x}_1 = 0$): We have $\dot{\sigma}(\tau) = \eta\dot{\delta}(\tau)$. Substituting this into (28) eliminates the set-valued parts, and the system can be reduced through summation to a single equation

$$\ddot{\delta}(\tau) + \delta(\tau) = -f(\tau) \Leftrightarrow \ddot{\delta}(\tau) = -\delta(\tau) - f(\tau) \tag{29}$$

which represents a forced oscillation with driving force $-f(\tau)$. Let $\tilde{f} := f_a/f_1$ be the normalized frequency of the applied field. Then, the steady-state solution can be written as

$$\delta(\tau) = A_0 + \sum_{n=1}^{2} \frac{A_n}{|1-(n\tilde{f})^2|} \sin(n\tilde{f}\tau + \pi/n - \varphi_n) \tag{30}$$

for $n = 1, 2$. For $\tilde{f} \to 1/n$, we observe resonant behavior, i.e., the amplitudes of the sin terms grow to infinity. The main resonance occurs for $n = 1$, and we designate by $\tilde{f}_1 := 1$ the tethered resonant frequency of the WRMMA. The numerical approximations of A_n are $A_0 \approx -(\mathcal{B}^2 + 0.81)$, $A_1 \approx 2.55\mathcal{B}$, and $A_2 \approx 0.81$.

4) Frequency Range for Stiction→Sliding Transition: We now derive the conditions on the driving frequency $\tilde{f}$ to transition the system from pure stiction to a sliding behavior, and thus to actual propulsion. Evaluating the stiction condition $|F_T| < \mu F_G$ in its nondimensional form and using (29) in the resulting inequalities yields the stiction condition

$$\Big|\delta(\tau) + f(\tau)\Big| < \frac{1}{\eta}. \tag{31}$$

Next, inserting (30) into (31) yields

$$\left|A_0 + \sum_{n=1}^{2} \frac{A_n}{|1-(n\tilde{f})^2|} \sin(n\tilde{f}\tau + \pi/n - \varphi_n) + f(\tau)\right| < \frac{1}{\eta}. \tag{32}$$

We observe that for $\tilde{f}$ which is sufficiently close to $1/n$, the term $A_n/|1-(n\tilde{f})^2|$ dominates the expression on the left. Then, because $|\sin(x)| \leq 1\,\forall x$, (32) reduces to

$$\frac{A_n}{|1-(n\tilde{f})^2|} < \frac{1}{\eta} \Longleftrightarrow |1-(n\tilde{f})^2| > \eta A_n \tag{33}$$

and the stiction conditions on $\tilde{f}$ are

$$\tilde{f} < \sqrt{\frac{1-\eta A_n}{n^2}} =: f_{1n}^{(s)}, \text{ and } \tilde{f} > \sqrt{\frac{1+\eta A_n}{n^2}} =: f_{2n}^{(s)}. \tag{34}$$

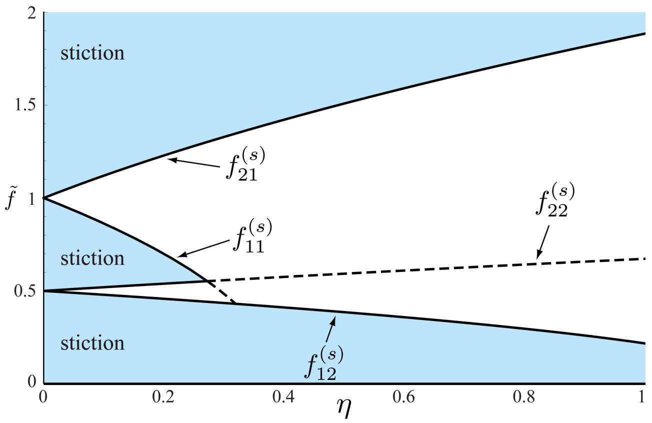

Fig. 4. Frequency range for stiction as a function of the nondimensional actuation and design parameter $\eta = F_0/\mu F_G$.

Fig. 4 shows the stiction areas in the $\tilde{f} - \eta$ diagram for $\mathcal{B} = 1$. For $\tilde{f}$ in the vicinity of $1/n$, the system will remain in stiction if $\tilde{f} < f_{1n}^{(s)}$ or if $\tilde{f} > f_{2n}^{(s)}$. If these conditions are not fulfilled, the system transitions into sliding. Thus, we have related a key parameter of the system η to the frequency ranges at which the WRMMA will move. The ratio $\eta = F_0/(\mu F_G)$ is a design and actuation parameter, since the magnetic force depends on the geometry of the magnetic bodies, as well as on the applied field strength, and the friction force depends on the properties of the involved surfaces but may also be varied through clamping.

5) Resonance During Sliding: During sliding we have $\dot{\sigma}(\tau) > \eta\dot{\delta}(\tau)$ or $\dot{\sigma}(\tau) < \eta\dot{\delta}(\tau)$, the friction force is maximum, and thus the inclusion system (28) can be written as a system of differential equations

$$\begin{cases}\ddot{\sigma}(\tau) - (\alpha-1)\eta\delta(\tau) + \gamma(\tau)\alpha = (\alpha-1)\eta f(\tau)\\ \ddot{\delta}(\tau) + (\alpha+1)\delta(\tau) - \gamma(\tau)\frac{\alpha}{\eta} = -(\alpha+1)f(\tau)\end{cases} \tag{35}$$

with $\gamma(\tau) := \operatorname{sgn}(\dot{\sigma}(\tau) - \eta\dot{\delta}(\tau)) = \pm 1$. We do not attempt to solve this coupled system, but rather derive its resonant behavior. For this, we note that the second equation does not involve $\sigma(\tau)$, and that it describes a driven linear oscillator. An analysis similar to the stiction case yields that during sliding, resonance occurs for $\tilde{f} \to \sqrt{1+\alpha}/n$. We define the main resonant frequency of the two-mass spring oscillator as

$$\tilde{f}_2 := \sqrt{1+\alpha} \tag{36}$$

i.e., increased by the factor $\sqrt{1+\alpha}$ compared to the stiction or tethered case (30). This increase is the cause of the experimentally observed increase in the driving actuation frequency of the WRMMA compared to the measured frequencies in the tethered case [7], [15].

To conclude, the analytical model, especially the conditions for the transition of stiction to sliding, is valid in the vicinity of $\tilde{f} \approx 1$. For the complete frequency range, a numerical investigation is required and the subject of the next section.

III. NONSMOOTH DYNAMICS OF THE WIRELESS RESONANT MAGNETIC MICROACTUATOR

To solve the equations of motion of the WRMMA without assumptions, we use the nonsmooth dynamics approach as described in [19]–[22]. This approach provides a mathematically sound formalism for the dynamics of rigid bodies with set-valued interaction laws for the description of unilateral contact, friction, and impact. Furthermore, Moreau's time-stepping method in combination with a linear complementary problem (LCP) formulation of the contact problem is used for the numerical simulation [21]. The main advantage of using this scheme over an event-driven algorithm is its robustness, as it does not require the explicit distinction between the impact, stick, and slip phases. In addition, the matrix/vector description and LCP formulation allow for a seamless extension to multiple contact points. Moreau's time-stepping method discretizes the equality of measures [18]

$$\mathbf{M}\mathrm{d}\mathbf{u} - \mathbf{h}(\mathbf{q}, \mathbf{u}, t)\mathrm{d}t - \sum \mathbf{w}_{Ni}\mathrm{d}P_{Ni} - \sum \mathbf{w}_{Ti}\mathrm{d}P_{Ti} = \mathbf{0} \tag{37}$$

which is a combined description of the nonimpulsive and impulsive motion. Here, $\mathrm{d}t$ is the Lebesgue measure on $\mathbb{R}$, $\mathbf{M} = \mathrm{diag}\,(m_B, m_B, m_H)$ is the constant mass matrix of the mechanical system, $\mathbf{u}$ are the velocities associated with the generalized coordinates $\mathbf{q}$, and $\mathbf{h}$ is the vector of noncontact forces such as spring, damper, and gravitational forces. The generalized force directions $\mathbf{w}_{Ni}$ and $\mathbf{w}_{Ti}$ and the percussion measures $\mathrm{d}P_{Ni}$ and $\mathrm{d}P_{Ti}$ describe the contribution of the contact forces/impulses to the dynamics of the system, with the subscripts N and T representing normal and tangential directions and i the contact number. The percussion measure P_i can be decomposed into a nonimpulsive contact force λ_i and the impulsive contact force Λ_i as

$$\mathrm{d}P_i = \lambda_i \mathrm{d}t + \Lambda_i \mathrm{d}\eta \tag{38}$$

where $\mathrm{d}\eta$ is the atomic differential measure. For more details on this formulation, see [19] and [20].

Fig. 2 recalls the free-body diagram of the WRMMA consisting of the body with coordinates (x_1, y_1) and the hammer with coordinate x_2. The generalized coordinates and the associated velocities are

$$\mathbf{q} = (x_1 \;\; y_1 \;\; x_2)^{\mathrm{T}}, \qquad \mathbf{u} = (v_{x,1} \;\; v_{y,1} \;\; v_{x,2})^{\mathrm{T}} \tag{39}$$

with $\dot{\mathbf{q}} = \mathbf{u}$ for almost all t. The system has a frictional contact between the body and the floor with a gap g_{N1}. We assume that this contact always remains closed, i.e., $g_{N1} = 0$, and, therefore, consider it to be a frictional bilateral contact with sliding velocity $\gamma_{T1}(\mathbf{u}) = v_{x,1}$ and friction coefficient μ. The friction force between the body and the substrate is λ_{T1}, and the reaction force of the substrate is λ_{N1}. Furthermore, there is a frictionless unilateral contact between the body and the hammer with gap $g_{N2} \geq 0$ and restitution coefficient ε. Since the contact is frictionless, we have $\lambda_{T2} = 0$; λ_{N2} is the contact force between the body and the hammer. The impulsive contact forces model the impact force between the body and the hammer considered only in the normal direction ($\Lambda_{N2} \geq 0, \Lambda_{T2} = 0$,) and its possible effect on the closed contact ($\Lambda_{N1} = 0, \Lambda_{T1} \geq 0$). The matrices $\mathbf{W}_N = (\,\mathbf{w}_{N1} \;\; \mathbf{w}_{N2}\,)$ and $\mathbf{W}_T = (\,\mathbf{w}_{T1} \;\; \mathbf{w}_{T2}\,)$ of generalized force directions are

$$\mathbf{W}_N = \begin{pmatrix} 0 & 1 & 0 \\ -1 & 0 & 1 \end{pmatrix}^{\mathrm{T}}, \qquad \mathbf{W}_T = \begin{pmatrix} 1 & 0 & 0 \\ 0 & 1 & 0 \end{pmatrix}^{\mathrm{T}}. \tag{40}$$

The noncontact forces $\mathbf{h}$ are the gravitational force $\mathbf{F}_G$, the clamping force $\mathbf{F}_C$, the spring force $\mathbf{F}_S$, damping $\mathbf{F}_D$, and magnetic force $\mathbf{F}_M$ between the body and the hammer, i.e.,

$$\mathbf{h} = \mathbf{F}_G + \mathbf{F}_C + \mathbf{F}_D + \mathbf{F}_M \tag{41}$$

which have been derived in Section II-A as

$$\mathbf{F}_G = (0 \quad -\beta(m_B + m_H)g \quad 0)^{\mathrm{T}} \tag{42}$$

$$\mathbf{F}_S(g_{N2}) = (\,-kg_{N2} \quad 0 \quad kg_{N2}\,)^{\mathrm{T}} \tag{43}$$

$$\mathbf{F}_D(\dot{g}_{N2}) = (\,c\dot{g}_{N2} \quad 0 \quad -c\dot{g}_{N2}\,)^{\mathrm{T}} \tag{44}$$

$$\mathbf{F}_m(g_{N2}, t) = (\,f_m(g_{N2}, t) \quad 0 \quad -f_m(g_{N2}, t)\,)^{\mathrm{T}} \tag{45}$$

$$\mathbf{F}_c(t) = (0 \quad -f_c(t) \quad 0)^{\mathrm{T}} \tag{46}$$

with

$$f_m(g_{N2}, t) = F_M(g_{N2})(\mathrm{sgn}\,(\sin(2\pi f_a t)) + \mathcal{B})^2 \tag{47}$$

$$f_c(t) = F_{\mathrm{C}0}(\mathrm{sgn}\,(\sin(2\pi f_a t + \varphi)) + 1)^2 \tag{48}$$

and $\mathcal{B} = 1$, unless otherwise specified. Note that in (42), β models unknown vertical forces and, thus, implicitly, the horizontal frictional force. We do not consider other unknown horizontal forces in this study.

A. Numerical Integration Procedure

Moreau's time-stepping method which is used to integrate (37) is a midpoint rule in which the percussions are solved for in an implicit way. First, a midpoint $\mathbf{q}_M$ of the generalized positions with a forward Euler step is calculated using the position and velocity at the beginning of the time step. The closed contacts are determined at $\mathbf{q}_M$. Then, the contact problem for the percussions of the closed contacts is set up in the form of an LCP. Solving the LCP gives an approximation of the velocity at the end of the time step. Finally, the positions are updated using the velocity at the end of the time step.

The integration scheme is implemented in MATLAB and is performed by sweeping over the actuation frequency f_a. In these parameter sweeps, the initial conditions at a specific frequency are the results of the simulation at the previous frequency. When sweeping the frequency in different directions, this may result in different steady-state solutions, i.e., it allows us to identify hysteresis in the system.

The goal parameter of interest in all of our studies is the mean velocity of the robot, which we define to be the mean

TABLE II
μMKSfA UNIT SYSTEM ALLOWS ONE TO STUDY PHENOMENA AT THE MICROSCALE WITHOUT NUMERICAL PROBLEMS

Parameter	MKS Unit	multiply by	to obtain µMKSfAUnit
Length	m	10^6	µm
Force	N	10^9	nN
Time	s	1	s
Mass	kg	10^3	g
Pressure	Pa	10^{-3}	kPa
Velocity	m/s	10^6	µm/s
Acceleration	m/s^2	10^6	µm/s^2
Density	kg/m^3	10^{-15}	g/µm^3
Mag. Field Intensity	A/m	10^9	fA/µm
Mag. Flux Density	T	10^{-12}	(no unit descr.)
Permeability	H/m	10^{-21}	(no unit descr.)

TABLE III
CONSTANT PARAMETERS THROUGHOUT THE SIMULATIONS

Parameter	Description	Value	Unit
L_{device}	total length of the device	300	µm
ρ_{Ni}	density of nickel	8900	kg/m^3
c	linear damping	1×10^{-3}	g/s
g_0	equilibrium gap	20	µm
μ	friction coefficient	0.5	-
ε	coefficient of restitution	0.5	-

displacement of the body per actuation period $T = 1/f_a$, i.e.,

$$u_{\text{robot}} := \frac{x_1(t+T) - x_1(t)}{T}. \tag{49}$$

For a given frequency, the number of periods for the integration procedure is determined iteratively until a convergence criteria is reached. This is either the absolute error threshold of 5×10^{-4} μm/s between two consecutive periods or the maximum number of iterations. The latter is 300 for the first frequency and then 100 for the next one. This ensures that the system has reached steady state and yields a good compromise between accuracy and computational time.

To avoid numerical problems due to small numbers, we describe the parameters in the scaled μMKSfA unit system as shown in Table II.[1] Since this uses μm as one of its base units, it represents a natural choice to model phenomena at the microscale. The time step for the integration dt is set to one thousandth of the actuation period, d$t = 10^{-3}T$, in order to ensure sufficient temporal resolution.

B. Parameter Sets

For the frequency sweeps, we typically scan a frequency range of $\tilde{f} \in \{0.3, 2.2\}$ in 75 equidistant steps. The investigated parameters are the mass ratio α, the strength of the magnetic field B, the friction β, and the effect of the periodic clamping force and its phase φ. Table III shows the parameters that are kept constant during the numerical analysis, such as the total length of the device as $L_{\text{device}} = 300\,\mu$m. The natural frequency is set to $f_n = 2300$ Hz, and the spring stiffness is calculated from $k = m_H(2\pi f_n)^2$.

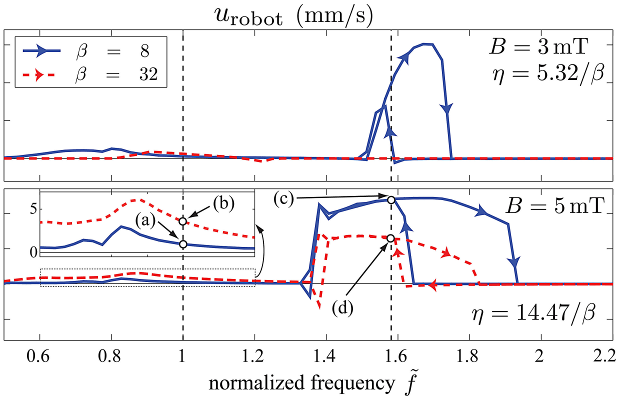

Fig. 5. Robot velocity for $\alpha = 1.5$ and $B = \{3, 5\}$ mT. The dashed vertical lines represent $\tilde{f}_1 = 1$ and $\tilde{f}_2 = 1.58$. The phase diagrams of points (a)–(d) are shown in Fig. 7.

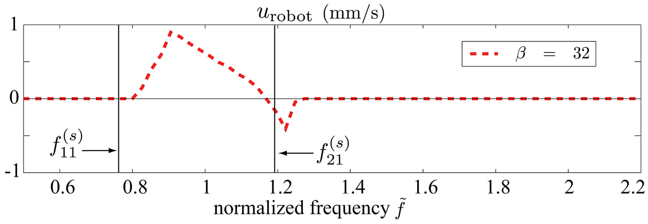

Fig. 6. Robot velocity for $B = 3\,$mT and $\alpha = 1.5$ ($\eta = 0.17$).

IV. NONSMOOTH DYNAMICS SIMULATION RESULTS

A. No Clamping: Natural Motion Principle

For the unclamped mode, Fig. 5 shows the results for $\alpha = 1.5$, $\beta = \{8, 32\}$, and $B = \{3, 5\}$ mT. The arrows indicate the direction of the frequency sweep. The vertical dashed lines are at the resonant frequencies $\tilde{f}_1$ and $\tilde{f}_2 = \sqrt{\alpha + 1} \approx 1.58$. We observe hysteretic motion around $\tilde{f}_2$: when sweeping up the frequency, motion starts at $\tilde{f} < \tilde{f}_2$ and stops at a frequency $\tilde{f} > \tilde{f}_2$. When sweeping down, the motion starts at $\tilde{f} \approx \tilde{f}_2$ and lasts until the starting frequency in the upsweeping case. This hysteretic behavior is consistent with empirical observations [7], and qualitatively validates the simulations.

Recall that β is used to model unknown vertical forces, and thereby varying frictional behavior, and note its unintuitive influence in Fig. 5. For $B = 5\,$mT, increasing β from 8 to 32 decreases the velocity at $\tilde{f}_2$, as one would expect. However, at $\tilde{f}_1$, the velocity is increased. This shows the importance of understanding and controlling the frictional behavior. This can be done statically by investigating different substrate materials [27], or dynamically, by applying a clamping force that is not sufficient to cause the body to stick to the substrate.

In Fig. 6, a closeup for the case $B = 3\,$mT and $\beta = 32$ is shown, together with the corresponding frequency limits for the actuation (34). We observe that the analytical limits correspond fairly well to the limits in the nonsmooth results, demonstrating its applicability. In addition, the motion is nonhysteretic, and the velocity changes direction as the frequency is changed, which is again, a behavior experimentally observed in [15].

---

[1] This table and other scaled unit systems can be found in the manual of the FE software ANSYS (www.ansys.com).

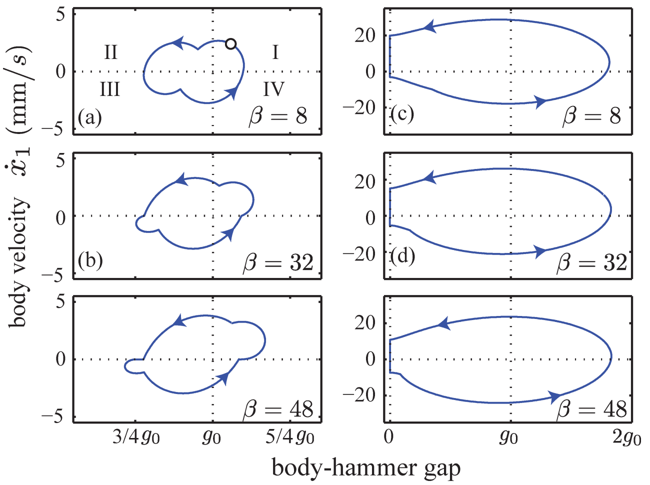

Fig. 7. Phase plots at $\tilde{f}_1$ (left column) and $\tilde{f}_2$ (right column). The points (a)–(d) correspond to those in Fig. 5 ($\alpha = 1.5$, $B = 5\,\mathrm{mT}$, $\eta = 14.79/\beta$).

The nonsmooth model allows one to investigate the motion principle using phase plots, such as in Fig. 7: For the points (a)–(d) in Fig. 5 and the additional case $\beta = 48$, the velocity $\dot{x}_1$ of the body versus the gap g_{N2} between the body and the hammer is shown. The arrows indicate the direction of motion in the phase space. The horizontal dotted line represents zero velocity of the body ($\dot{x}_1 = 0$), and the vertical dotted lines represent the equilibrium gap g_0 and the closed gap (only in the right column). Consider the plot for point (a) (top left), and assume that motion starts in quadrant I at the marked point. In I, the gap reduces, while the body moves in the positive direction ($\dot{x}_1 > 0$). In II, the gap further reduces, while the body velocity mainly decreases to zero and changes direction in III. The change of velocity occurs at a nonzero gap, i.e., without impact. The motion in III and IV is opposed to I and II, i.e., the gap increases, while the body moves in the negative direction. Thus, for this configuration, the body oscillates in a pure sliding motion. Now consider the case for $\tilde{f}_1$ and significantly increased friction, $\beta = 48$ (bottom left). The general oscillatory behavior is the same as in the previous case. However, at the transition from II to III, the body velocity remains zero, while the gap is further reducing. This indicates stiction of the body and a general stick/slip motion.

In contrast, consider any configuration of $\tilde{f}_2$ (right column). The gap closes completely in II, and the body velocity jumps from a positive value in II to a negative value in III, indicating that impact occurred. Note, however, that the occurring impact does not mean that the body is pushed forward by the hammer. In fact, the corresponding velocities in Fig. 5 are positive, indicating that the hammer is pulling the body. These findings are in clear contrast with the speculations in [7] and [15], where it is assumed that the impact of the hammer onto the body breaks the static friction of the body and moves it forward, e.g., the hammer *pushes* the body. Instead, our results indicate that the natural motion of the WRMMA occurs by pure sliding, stick/slip motion of the body, or impact. Even for impact, though, the hammer *pulls* the body. In addition, friction seems to have little effect on the motion mechanism, as the phase diagrams for $\tilde{f}_2$ are qualitatively identical for varying friction, and for $\tilde{f}_1$, the motion mechanism transitions from pure sliding to stick/slip motion with increasing β.

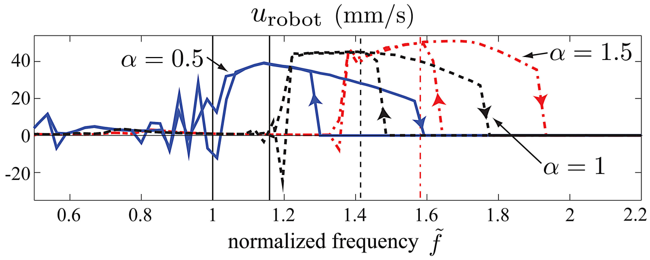

Fig. 8. Effect of the mass ratio α. The actuation range around the decreasing resonant frequency $\tilde{f}_2 = \sqrt{1+\alpha}$ (vertical lines) merges with the one around $\tilde{f}_1$ and results in erratic behavior for small α ($\beta = 8$, $B = 5\,\mathrm{mT}$, and $\eta = 1.85$).

B. Mass Ratio and Design for Multiagent Control

Fig. 8 shows the effect of the mass ratio α. Note that the resonant frequencies $\tilde{f}_2 = \sqrt{1+\alpha}$ for the two-mass spring oscillator decrease with decreasing α. As the actuation range around those frequencies is relatively large, these areas merge with the actuation areas around $\tilde{f} = 1$ for small α, and an erratic behavior emerges.

Fig. 8 is also interesting in view of multiagent control, i.e., where multiple devices are actuated on the same substrate. In [15], it is suggested that this is possible if the resonant frequencies of the individual devices are sufficiently different. Our results in Fig. 8 show that the actuation areas are relatively large and may overlap even for designs that are significantly different. This frequency range must be taken into account for successful design. One possibility is to decrease the actuation field strength as this decreases the actuation range and, thus, allows for better separation (see Fig. 5).

C. Effect of Clamping: Velocity Control

Fig. 9 shows the results when a periodic clamping force (48) with a phase shift φ with respect to the magnetic signal is applied to the body. The other parameters are set as $\alpha = 1.5$, $B = 5\,\mathrm{mT}$, and $\beta = 8$. The respective curve for the no-clamping case from Fig. 5 is shown as a reference. We observe that the actuation range is increased with the maximum velocity shifting from $\tilde{f}_2 \approx 1.58$ to $\tilde{f} \approx 1.2$. The net velocities around $\tilde{f} = 1.58$ are reduced, and around $\tilde{f} = 1.2$, they are significantly larger compared to the unclamped case. A slight hysteresis is observed for $\varphi = \pi/2$ around $\tilde{f} = 1.1$. Clearly, changing φ from $-\pi/2$ to $\pi/2$ reverses the direction of the velocity. The motion in these cases is rather smooth and changes direction at $\tilde{f} \approx 1.35$, when motion in the unclamped case starts. These effects have been described previously [15]. Yet, this downshift of the actuation frequency shown by our model was wrongly interpreted in [15] as an actual increase of the actuation frequency compared with the tethered mode, as mentioned in Section II-B5.

Next, in Fig. 10 the continuous variation of φ is shown for the case $\tilde{f} = 1.58$ of Fig 9. We see that a phase shift from $-\pi/2$ to $\pi/2$ induces a change in the velocity direction with

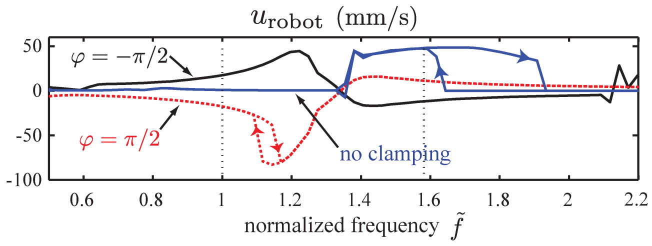

Fig. 9. Effect of the clamping signal. The actuation range is shifted to lower frequencies, and the direction of velocity is changed at $\tilde{f} \approx 1.35$ ($\alpha = 1.5$, $B = 5\,\text{mT}$, and $\beta = 8$).

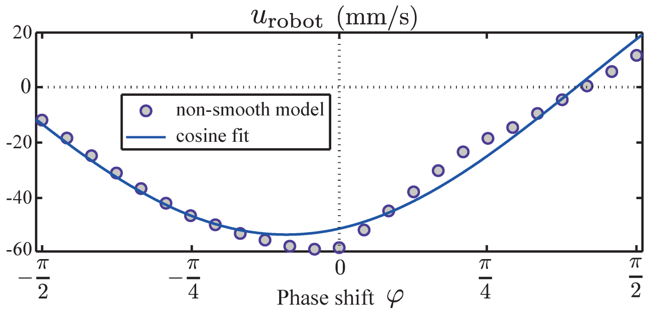

Fig. 10. Influence of the clamping phase shift φ on the velocity ($\beta = 8$, $\tilde{f} = 1.58$, and $B = 5\,\text{mT}$).

approximately the same magnitude. However, the change is not sharp, but rather shows a cosine behavior. Thus, the model predicts that it is possible to control both the magnitude and the direction of the velocity through φ. This cosine behavior of the velocity with φ is well supported by experiments [27] validating our results.

Both the rectification and smoothness of motion when clamping is activated can be explained in the phase plot shown in Fig. 11. We can identify the impact for the no-clamping case by the velocity jump at $g_{N2} = 0$. However, in the clamping cases, the gap never closes, and we see stick/slip motion with nonzero body velocity primarily in one direction, e.g., positive for $\varphi = \pi/2$. Thus, the motion of the body has been rectified. The smoothness is a result of the rectification as the body no longer oscillates. Thus, the clamping force changes the motion mechanism from impact to stick/slip driven motion.

This analysis indicates that clamping has a different effect of what has been speculated in [7] and [15]. There, it was observed that the net velocity increases with clamping, which is also verified in our model. However, it was thought that the reason for this increase was that clamping down the body allowed for larger impact velocities and, thus, larger propulsion of the robot. However, our results indicate that the effect of clamping is different. At frequencies with small or zero velocities in the unclamped case (e.g., $\tilde{f} \in (1, 1.2)$ in Fig. 9), the rectification of the oscillation of the body allows for an efficient energy transfer, and thus larger net velocities. At frequencies where impact occurred in the unclamped case (e.g., $\tilde{f} = 1.58$ in Fig. 9), the impact is eliminated by clamping, and the motion mechanism is changed to a stick/slip motion.

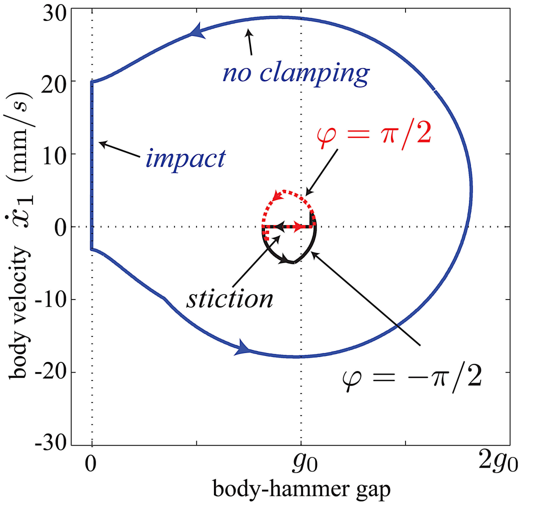

Fig. 11. We see that clamping changes the motion mechanism fundamentally from impact driven to a stick/slip motion ($\alpha = 1.5, B = 5\,\text{mT}, \beta = 8$, and $\tilde{f} = 1.58$).

V. SUMMARY AND DISCUSSION

In this paper, we have applied nonsmooth multibody dynamics to describe the motion of complex microrobots that exhibit friction and impact. As an example, we studied the WRMMA that is driven by oscillating magnetic fields. We analyzed the system analytically and derived the interaction forces and frequency limits for actuation. We integrated the nonsmooth equations of motion numerically using Moreau's time-stepping scheme. Our results are qualitatively consistent with experimental observations [7], [15], and predict the magnitude of the velocities, hysteretic motion, and the change of the direction of the velocity with changing frequency.

Our results provide further insight into the motion of resonant microrobots. In contrast with previous speculations that the WRMMA behaves as an impact drive actuator, our results show that the WRMMA is a two-mass spring oscillator, and its natural motion principle is stick/slip behavior. The stiction and sliding phases are governed by the actuation frequency and the friction. Our results also predict impact around the resonant frequency of the oscillator. However, this impact does not contribute to propulsion. Finally, our results explain how the clamping force acts to increase the actuation range, to rectify the oscillations of the body, and, thereby, to smoothen the motion of the WRMMA.

As mechanical systems with friction and frictional impacts are among the most complex mechanical systems to analyze, the method that is described in this paper applies to a large range of different robots and will guide engineers and researchers through their design and actuation phase.

REFERENCES

[1] B. J. Nelson, I. K. Kaliakatsos, and J. J. Abbott, "Microrobots for minimally invasive medicine," *Annu. Rev. Biomed. Eng.*, vol. 12, pp. 55–85, Jun. 2010.

[2] J. J. Abbott, Z. Nagy, F. Beyeler, and B. J. Nelson, "Robotics in the small—Part I: Microrobotics," *IEEE Robot. Automat. Mag.*, vol. 14, no. 2, pp. 92–103, Jun. 2007.

[3] B. Donald, C. Levey, C. McGray, D. Rus, and M. Sinclair, "Power delivery and locomotion of untethered microactuators," *J. Microelectromech. Syst.*, vol. 12, no. 6, pp. 947–959, 2003.

[4] A. Yamazaki, M. Sendoh, K. Ishiyama, K. Arai, R. Kato, M. Nakano, and H. Fukunaga, "Wireless micro swimming machine with magnetic thin film," *J. Magn. Magn. Mater.*, vol. 272, pp. E1741–E1742, 2004.

[5] K. B. Yesin, K. Vollmers, and B. J. Nelson, "Modeling and control of untethered biomicrorobots in a fluidic environment using electromagnetic fields," *Int. J. Rob. Res.*, vol. 25, no. 5–6, pp. 527–536, 2006.

[6] O. J. Sul, M. R. Falvo, I. R. M. Taylor, S. Washburn, and R. Superfine, "Thermally actuated untethered impact-driven locomotive microdevices," *Appl. Phys. Lett.*, vol. 89, pp. 203512-1–203512-3, 2006.

[7] K. Vollmers, D. R. Frutiger, B. E. Kratochvil, and B. J. Nelson, "Wireless resonant magnetic microactuator for untethered mobile microrobots," *Appl. Phys. Lett.*, vol. 92, no. 14, pp. 144103-1–144103-3, 2008.

[8] C. Pawashe, S. Floyd, and M. Sitti, "Modeling and experimental characterization of an untethered magnetic micro-robot," *Int. J. Robot. Res.*, vol. 28, no. 8, pp. 1077–1094, 2009.

[9] K. Ishiyama, K. I. Arai, M. Sendoh, and A. Yamazaki, "Spiral-type micromachine for medical applications," *J. Micromechatronics*, vol. 2, no. 1, pp. 77–86, 2003.

[10] L. Zhang, J. J. Abbott, L. X. Dong, B. E. Kratochvil, D. J. Bell, and B. J. Nelson, "Artificial bacterial flagella: Fabrication and magnetic control," *Appl. Phys. Lett.*, vol. 94, no. 6, pp. 064107-1–064107-3, 2009.

[11] T. Akiyama and K. Shono, "Controlled stepwise motion in polysilicon microstructures," *J. Microelectromech. Syst.*, vol. 2, no. 3, pp. 106–110, 1993.

[12] B. Donald, C. Levey, C. McGray, I. Paprotny, and D. Rus, "An untethered, electrostatic, globally controllable MEMS micro-robot," *J. Microelectromech. Syst.*, vol. 15, no. 1, pp. 1–15, 2006.

[13] B. Donald, C. Levey, and I. Paprotny, "Planar microassembly by parallel actuation of MEMS microrobots," *J. Microelectromech. Syst.*, vol. 17, no. 4, pp. 789–808, 2008.

[14] S. Floyd, E. Diller, C. Pawashe, and M. Sitti, "Control methodologies for a heterogeneous group of untethered magnetic micro-robots," *Int. J. Robot. Res.*, vol. 30, no. 13, pp. 1553–1565, 2011.

[15] D. R. Frutiger, B. E. Kratochvil, K. Vollmers, and B. J. Nelson, "Small, fast, and under control: Wireless resonant magnetic micro-agents," *Int. J. Robot. Res.*, vol. 29, no. 5, pp. 613–636, 2010.

[16] D. R. Frutiger, B. E. Kratochvil, and B. J. Nelson, "MagMites—Microrobots for wireless microhandling in dry and wet environments," in *Proc. IEEE Int. Conf. Robot. Automat.*, May 2010, pp. 1112–1113.

[17] B. Brogliato, A. ten Dam, L. Paoli, F. Génot, and M. Abadie, "Numerical simulation of finite dimensional multibody nonsmooth mechanical systems," *Appl. Mech. Rev.*, vol. 55, no. 2, pp. 107–150, 2002.

[18] J. Moreau, "Unilateral contact and dry friction in finite freedom dynamics," in *Non-Smooth Mechanics and Applications* (ser. CISM Courses and Lectures), vol. 302, J. Moreau and P. Panagiotopoulos, Eds. Wien, Vienna: Springer-Verlag, 1988, pp. 1–82.

[19] C. Glocker, *Set-Valued Force Laws* (ser. Lecture Notes in Applied Mechanics), vol. 1, Berlin, Germany: Springer, 2001.

[20] R. Leine and H. Nijmeijer, *Dynamics and Bifurcations of Non-Smooth Mechanical Systems* (ser. Lecture Notes in Applied and Computational Mechanics), vol. 18, Berlin, Germany: Springer, 2004.

[21] C. Glocker and C. Studer, "Formulation and preparation for numerical evaluation of linear complementarity systems in dynamics," *Multibody Syst. Dyn.*, vol. 13, no. 4, pp. 447–463, 2005.

[22] R. Leine and N. van de Wouw, *Stability and Convergence of Mechanical Systems With Unilateral Constraints* (ser. Lecture Notes in Applied and Computational Mechanics), vol. 36, Berlin, Germany: Springer, 2008.

[23] A. A. Transeth, R. I. Leine, C. Glocker, and K. Y. Pettersen, "3-D snake robot motion: Nonsmooth modeling, simulations, and experiments," *IEEE Trans. Robot.*, vol. 24, no. 2, pp. 361–376, Apr. 2008.

[24] L. Tching and G. Dumont, "Haptic simulations based on non-smooth dynamics for rigid-bodies," in *Proc. 2008 ACM Symp. Virtual Reality Software Technol.*, 2008, pp. 87–90.

[25] M. Möller and C. Glocker, "Non-smooth modelling of electrical systems using the flux approach," *Nonlinear Dyn.*, vol. 50, pp. 273–295, 2007.

[26] Z. Nagy, D. R. Frutiger, R. I. Leine, C. Glocker, and B. J. Nelson, "Modeling and analysis of wireless resonant magnetic microactuators," in *Proc. IEEE Int. Conf. Robot. Automat.*, May 2010, pp. 1598–1603.

[27] D. R. Frutiger, "MagMites," Ph.D. dissertation, ETH Zurich, Zurich, Switzerland, 2010, doi:10.3929/ethz-a-006510916.

[28] E. P. Furlani, *Permanent Magnet and Electromechanical Devices*. San Diego, CA: Academic, 2001.

[29] S. Brugger and O. Paul, "Magnetic field amplification by slender cuboid-shaped magnetic concentrators with a single gap," *Sens. Actuators A: Phys.*, vol. 157, no. 1, pp. 135–139, 2010.

[30] J. J. Abbott, O. Ergeneman, M. P. Kummer, A. M. Hirt, and B. J. Nelson, "Modeling magnetic torque and force for controlled manipulation of soft-magnetic bodies," *IEEE Trans. Robot.*, vol. 23, no. 6, pp. 1247–1252, Dec. 2007.

[31] M. Beleggia, M. De Graef, and Y. T. Millev, "The equivalent ellipsoid of a magnetized body," *J. Phys. D*, vol. 39, no. 5, pp. 891–899, 2006.

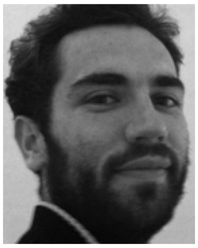

Zoltán Nagy received the Diploma and Ph.D. degrees in mechanical engineering from ETH Zurich, Zurich, Switzerland, in 2006 and 2011, respectively. His Ph.D. research focused on modeling the magnetization and the dynamics of untethered magnetic microrobots. He also investigated magnetic self-assembly for swallowable modular robots, both experimentally and theoretically.

He is currently a Postdoctoral Researcher with the Institute of Technology in Architecture, ETH Zurich, where he is interested in practical applications of artificial intelligence in building systems. His research interests are interdisciplinary and include multiphysics modeling and control of complex systems.

Remco I. Leine received the M.Sc. degree from the Delft University of Technology, Delft, The Netherlands, and the Ph.D. degree from the Eindhoven University of Technology, Eindhoven, The Netherlands, in 1996 and 2000, respectively, both in mechanical engineering. He received the Habilitation degree from the ETH Zurich in 2007 and was appointed as a Privatdozent for Mechanics

He was a Postdoctoral Researcher with the Technical University Munich Germany, the Institut National de Recherche en Informatique et Automatique (INRIA) Rhône-Alpes, Grenoble, France, and the ETH Zurich, Zurich, Switzerland. He was granted a fellowship from the Royal Dutch Academy of Sciences in 2002. Since 2003, he has been with the Institute of Mechanical Systems, ETH Zurich. He is currently a Titular Professor with the Institute of Mechanical Systems. His research interests include the intersection of nonsmooth dynamics and nonlinear dynamics: stability theory for nonsmooth systems, friction-induced vibration and nonlinear phenomena, discontinuous bifurcations in nonsmooth dynamical systems, and multibody systems with impact and friction.

Dominic R. Frutiger (M'11) received the Diploma and Ph.D. degrees in mechanical engineering from ETH Zurich, Zurich, Switzerland, in 2004 and 2010, respectively. During his studies, he was involved in interdisciplinary projects ranging from artificial intelligence and artificial evolution over synthetic biology to semiconductor nanocrystals on carbon nanotubes as basic building blocks in micro- and nanorobotics.

Since the beginning of the team effort in November 2006, he has been designing the MagMite agents based on the wireless resonant magnetic microactuator actuation principle for dry and wet applications. He is currently a postdoctoral researcher at the Institute of Robotics and Intelligent Systems, ETH Zurich.

Christoph Glocker received the Diploma and Doctoral degrees in mechanical engineering, and the Certificate of Habilitation in mechanics, from the Technische Universität München (TUM), Munich, Germany, in 1989, 1995, and 2001, respectively.

In 1996, he was granted a Feodor Lynen fellowship supported by the Alexander von Humboldt Foundation and spent one year at Aristotle University of Thessaloniki, Thessaloniki, Greece. In 1997, he joined TUM as a Senior Engineer. He then joined ETH Zurich, Zurich, Switzerland, where he is currently a Full Professor of Mechanics with the Institute of Mechanical Systems. He is involved in the research of nonsmooth dynamics of mechanical systems with finite degrees of freedom that includes, for example, the friction and impact problem in multibody systems, providing a generalization of classical analytical mechanics. His current research interests also include both theoretical and practical questions concerning the mechanical modeling, the mathematical formulation, and the numerical treatment of systems with discontinuities, as well as their applications to industrial problems.

Bradley J. Nelson (M'90–SM'06–F'11) received the Ph.D. degree in robotics from Carnegie Mellon University, Pittsburgh, PA, in 1995.

In 1995, he became an Assistant Professor with the University of Illinois, Chicago, and an Associate Professor with the University of Minnesota, Minneapolis, in 1998. In 2002, he was a Professor of robotics and intelligent systems with ETH Zurich, Zurich, Switzerland, where he is currently the Head of the Institute of Robotics and Intelligent Systems, as well as the Chairman of the ETH Electron Microscopy Center. His research interests include microrobotics and nanorobotics.

Dr. Nelson was named to the 2005 Scientific American 50. His laboratory won the biennial RoboCup Nanogram competition in 2007 and 2009. He is also the recipient of multiple best conference paper awards, and one of his mirorobots appears in the 2012 Guinness Book of World Records as the "Most Advanced Mini Robot for Medical Use."